nature physics

Article

https://doi.org/10.1038/s41567-026-03215-5

Active assembly and non-reciprocal dynamics of elastic membranes

Received: 10 October 2025

Accepted: 9 February 2026

Published online: 02 April 2026

Check for updates

John Berezney[1,2,8], Sattvic Ray[2,8], Itamar Kolvin[3,8], Fridtjof Brauns[2,4], Sihan Chen[5,6], Mark Bowick[2,4], Seth Fraden[1], Vincenzo Vitelli[5,6] & Zvonimir Dogic[2,7]

Equilibrium self-assembly and conventional materials processing techniques fall far short of mimicking dynamic self-actuating processes that are commonplace throughout biology. Here, to bridge the gap between living and synthetic matter, we study passive adhesive non-thermal actin fibres immersed in an active microtubule-based fluid. We show that autonomous chaotic flows power non-equilibrium fibre dynamics, thus inducing collisions, generating connections and weaving a membrane-like elastic network. The ensuing active assembly generates a hierarchy of shapes, structures and dynamical processes spanning nanometres to centimetres. Ultimately, it generates an active membrane that exhibits global limit cycles induced by a non-reciprocal coupling between deformations of the elastic membrane and the alignment axis of the nematic active fluid. Our work merges self-assembly with active matter to demonstrate self-processing materials wherein hierarchical life-like structures and dynamics emerge from an initially structureless suspension.

During biological development, complex forms and functions emerge from an embryo that lacks large-scale structure. Morphogenesis is underlined by inscribing in-plane strains into elastic epithelial sheets, which causes them to form complex tissues, organs and whole organisms[1,2]. Translating such complex yet robust self-organizing processes into the realm of materials science presents an opportunity to generate dynamical materials that are not accessible using paradigms of equilibrium self-assembly and conventional materials processing through external energy input. In equilibrium self-assembly, free-energy-minimizing structures emerge from a structureless suspension of microscopic particles with well-defined interactions. Although capable of generating intricate structures[3–6], self-assembly requires well-tuned conditions and microscopic building blocks that exhibit thermal motion. When local barriers in the free-energy landscape exceed the accessible thermal energy, intermediate states become kinetically trapped, and self-assembly fails to reach the target structure[7,8]. Finally, conventional self-assembly yields only static materials that lack the alluring dynamics and unique mechanical properties observed in living matter. To overcome these intrinsic limitations of equilibrium, living matter assembles dynamical and reconfigurable structures through a continuous input of microscopic energy[9,10]. In synthetic systems, a non-equilibrium drive can be generated with active fluids built from energy-consuming components[11–14]. Active fluids exhibit autonomous chaotic flows that drive the motion of passive embedded objects, which allows them to efficiently explore the phase space[12,15–17]. In turn, such non-equilibrium dynamics can bring together attractive passive particles to generate and grow structures and to actuate their dynamical soft modes[18–22].

We study the active assembly of filamentous actin networks crosslinked with the protein fascin. Previous efforts explored the range of accessible structural and mechanical properties when such systems are assembled by thermal fluctuations. In the thermal limit,

[1]Department of Physics, Brandeis University, Waltham, MA, USA. [2]Department of Physics, University of California at Santa Barbara, Santa Barbara, CA, USA. [3]School of Physics, Georgia Institute of Technology, Atlanta, GA, USA. [4]Kavli Institute of Theoretical Physics, Santa Barbara, CA, USA. [5]Leinweber Institute for Theoretical Physics, University of Chicago, Chicago, IL, USA. [6]James Frank Institute, University of Chicago, Chicago, IL, USA. [7]Interdisciplinary Program in Quantitative Biosciences, University of California, Santa Barbara, CA, USA. [8]These authors contributed equally: John Berezney, Sattvic Ray, Itamar Kolvin. e-mail: zdogic@physics.ucsb.edu

https://doi.org/10.1038/s41567-026-03215-5

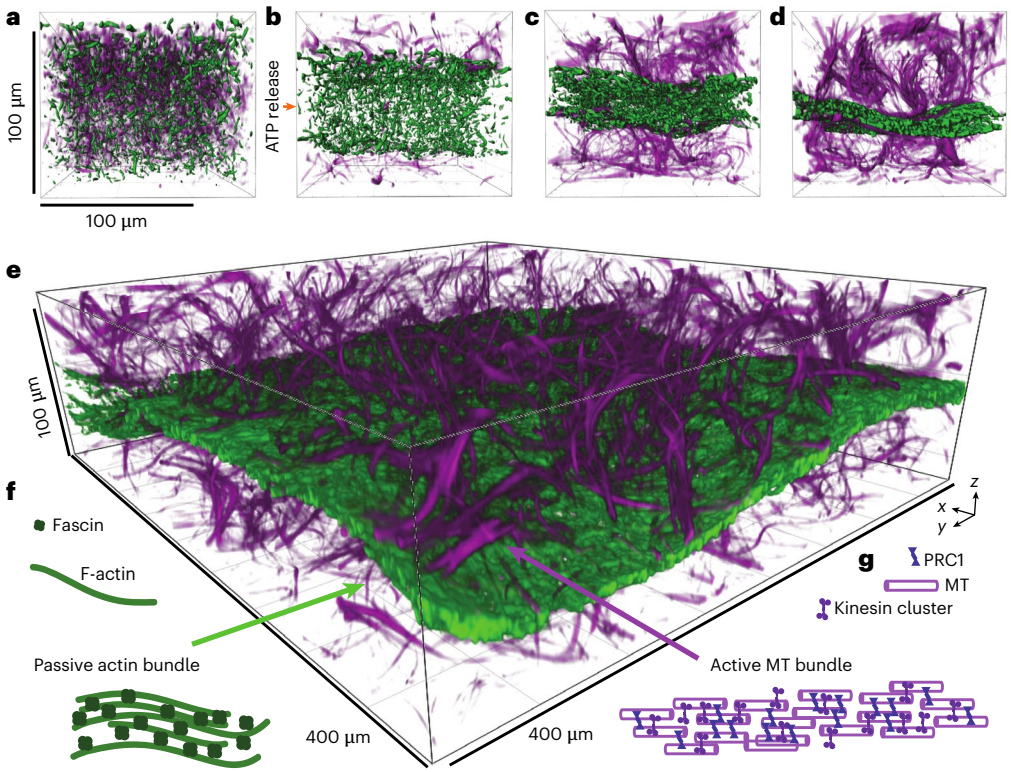

Fig. 1 | Active assembly of elastic membranes. a–**d**, Active MT bundles (magenta) drive fascin-linked actin bundles (green) into an elastic membrane. Snapshots at 00:00:00 (**a**), 00:35:48 (**b**), 01:12:50 (**c**) and 1:49:53 (**d**). **e**, A larger section of the actin membrane surrounded by MT bundles. **f**, Passive F-actin bundles crosslinked with fascin. **g**, The active fluid consists of MTs, MT-specific bundler PRC1 and kinesin–streptavidin clusters. The sample is in low-salt active buffer 1 (Supplementary Information). Actin concentration 4.0 µM.

the network morphology is determined not only by the filament and crosslinker concentration but also critically depends on kinetic factors that arise from the competition between filament growth, diffusion and steric hindrance[23–26]. We explore distinct non-thermal pathways for the assembly of actin networks by merging passive actin network components with a microtubule (MT)-based active fluid. Advected by the MT-generated chaotic flows, actin filaments collide with one another and then link together to form permanent connections to generate a network-like structure. In the ensuing active assembly process, the emergent actin-based elastic structures exert feedback on the MT-based active drive, which initiates a multiscale cascade of interacting structural and dynamical processes. Ultimately, we observe the robust emergence of actin-based elastic membranes, which exhibit system-sized limit-cycle oscillations generated by a non-reciprocal coupling between the in-plane actin displacement and the MT tilt. These observations reveal the potential of active assembly, wherein, like biological morphogenesis, complex life-like materials emerge from an initial structureless mix of active and passive components.

Active assembly of elastic membranes

To investigate how active stresses organize adhesive filaments, we constructed a composite system in which MT-based active fluid sterically and hydrodynamically interacted with actin and its crosslinker fascin in active buffer 1 (Fig. 1f,g and Supplementary Methods). Before the initiation of activity, fascin-crosslinked actin and PRC1-bundled MTs formed an interpenetrating double network that had negligible thermal fluctuations and was static for days[27]. Upon release of caged ATP, kinesin–streptavidin motor clusters drove MT bundle extension, leading to persistent chaotic flows[12]. In turn, these flows robustly assembled the actin filaments into a thin elastic membrane at the chamber midplane. Active MT bundles segregated above and below the actin membrane and drove its elastic deformations (Fig. 1a–e and Supplementary Video 1). The non-equilibrium membrane fluctuations persisted until the ATP was exhausted, which demonstrates that the active fluid both assembled an elastic membrane and actuated its dynamics. The membrane assembly was a consequence of the anisotropic confinement geometry; isotropic confinements generated isotropic contractions.

To focus on the initial stages of active assembly, we reduced the actin concentration to 1.5 µM (from 4.0 µM in Fig. 1). In this regime, the initial state consisted of well-separated actin bundles or locally connected clusters of bundles that could be segmented (Fig. 2a). ATP release generated flows that advected the filamentous actin, causing their enhanced motion, collisions and the formation of irreversible fascin-crosslinked junctions. The low actin density revealed the temporal evolution of the three-dimensional (3D) network connectivity and cluster size distribution over time. The driven dynamics increased the size of the largest cluster in the first 2 min, culminating in the formation of a globally percolated structure (Fig. 2b,c). Usually, percolation arises from thermally driven cluster aggregation. By contrast, the percolation of active bundles is orchestrated by spatio-temporally correlated active flows. After the percolation transition, activity drove further network rearrangements for the next 20 min. Ultimately, it generated a heterogeneous membrane-like network in which a fraction of the filamentous material merged to form brighter and thicker bundles connected through well-defined nodes (Fig. 2d and Supplementary Video 2).

The network structure was strongly influenced by the actin concentration. At an even lower initial actin bundle density (1.0 µM), active flows assembled a percolated structure that had a large mesh size (Supplementary Video 3). Once assembled, the active fluid continued to excite large-amplitude network deformations. The resulting dynamics indicates that at low actin concentration, the large-mesh network lacks rigidity (finite elastic modulus) at low strains.

https://doi.org/10.1038/s41567-026-03215-5

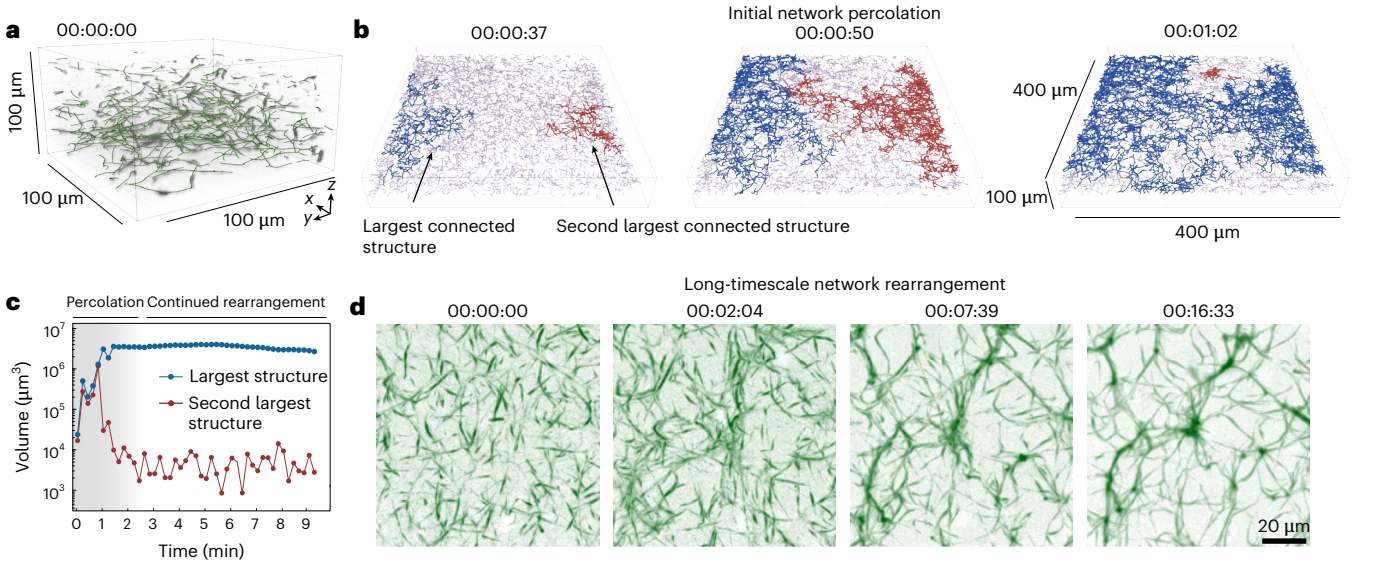

Fig. 2 | Active assembly from preformed bundles. a, An initial state consists of well-separated disconnected actin bundles. **b**, Activity drives bundle dynamics to rapidly form connected domains. The largest and second largest connected domains are in blue and red, whereas the others are in grey. **c**, Time evolution of the largest and second largest connected domains. **d**, The *z*-projection of the actin network. After geometrical percolation, which occurs within 2 min, the network continued coarsening, as evidenced by qualitative changes in its appearance. 1.5 µM actin, 0.5 µM fascin in active buffer 1.

Active assembly yields membranes over a wide range of initial conditions. We also studied samples in the high-salt active buffer 2. In this buffer, actin (1.5 µM) and fascin formed a homogeneous network of crosslinked unbundled filaments instead of the above-described heterogeneous network of bundles assembled in the low-salt active buffer 1. Before sample activation, the actin fluorescence intensity was uniform, as the individual filaments were not spatially resolvable on optical length scales (Fig. 3a, left). For 2 h post-initiation, the unbundled actin filaments were fluidized by chaotic MT flows without forming stable contacts and actin fluorescence remained uniform. Afterwards, we observed the gradual appearance of actin bundles that became thicker over time (Fig. 3a, centre and right, and Supplementary Video 4). Such dynamics was reflected in the variance of actin fluorescence intensity, which continued increasing until 5 h after sample activation (Fig. 3d, black curve). Concomitantly, actin began contracting towards the sample midplane, as evidenced from a side view (Fig. 3b). We quantified membrane formation by segmenting the actin layer at each time point and computing its mean thickness over the field of view (Supplementary Methods). The membrane thickness decreased steadily between hours 2 and 10 (Fig. 3d, blue curve). The delayed development of the membranous network indicates that actin bundle formation involves a kinetic barrier that cannot be traversed by thermal fluctuations alone[24–26], for these experimental conditions. Active flows enhance the filament collisions and alignments, enabling the transition into the lower-energy bundled state.

The assembling actin network generated passive stresses that influenced the MT-based flow fields. We computed the spatially averaged mean actin and MT speed as a function of time (Fig. 3e). Initially, both MTs and actin moved at ~0.5 µm s^{-1}. After 2 h, concomitant with bundle formation and network contraction, both components slowed down to ~0.15 µm s^{-1}. On its own, the MT–kinesin active fluid exhibit constant steady-state speed over its lifetime[28]. Thus, the rapid slowdown of the composite dynamics after 2 h indicates feedback of the emerging elastic actin–fascin network to the active fluid.

To further evaluate the coupling between passive and active components, we measured the spatial autocorrelation of the MT and actin velocity fields and extracted their characteristic length scales (Fig. 3c, centre and right, and Supplementary Methods). Throughout the sample lifetime, MTs exhibited chaotic short-range flows, reflected in a constant ~100 µm correlation length (Fig. 3f, pink curve). Before network formation, the actin and MT velocity fields had comparable length scales. After 2 h, however, the actin flows became correlated over increasingly larger length scales, with the correlation length reaching ~800 µm (Fig. 3f, green curve). The divergence between active and passive length scales demonstrates that short-range active stresses drove increasingly long-range deformations of the emergent elastic membrane. Both the slowdown in the average speed and the divergence between MT and active flow fields indicate the emergence of network elasticity. The overall dynamics is determined by the balance of MT-generated active stresses and passive stresses, the latter probably dominated by the deforming actin network. The assembling passive network generates increasingly larger passive stresses that resist active stresses. Being composed of inextensible actin bundles, the elastic network cannot follow the chaotic MT flows, thus forcing correlated displacements across the membrane. These results demonstrate that the active assembly of membranes is a robust process that can occur from both bundled and unbundled initial states.

Active buckling

Once fully formed, active fluid actuated the out-of-plane bending fluctuations of the solid membrane (Fig. 4a,b and Supplementary Video 5). To characterize these active fluctuations, we reconstructed the membrane midsurface $h(x, y, t)$ from the actin fluorescence intensity (Fig. 4a,b) and quantified its spatially averaged thickness and root-mean-squared height fluctuation (Fig. 4d). The membrane thickness stabilized within an hour. In comparison, the height fluctuations steadily increased in amplitude whereas their temporal relaxation slowed down (Fig. 4c).

The out-of-plane membrane motion was driven by the surrounding extensile MT bundles. MTs impinging on the membrane at a steep angle could directly drive out-of-plane motion (Fig. 4e, top). Alternatively, they could exert in-plane forces, locally compressing the membranes and causing them to bend and buckle (Fig. 4e, top). To distinguish these two scenarios, we quantified the relation between the membrane bending, calculated from the reconstructed midsurfaces (Fig. 4h), and its in-plane deformation, calculated from tracked nodes in the actin network (Supplementary Video 6 and Supplementary Methods). The in-plane strain was dominated by compression, which ranged between

https://doi.org/10.1038/s41567-026-03215-5

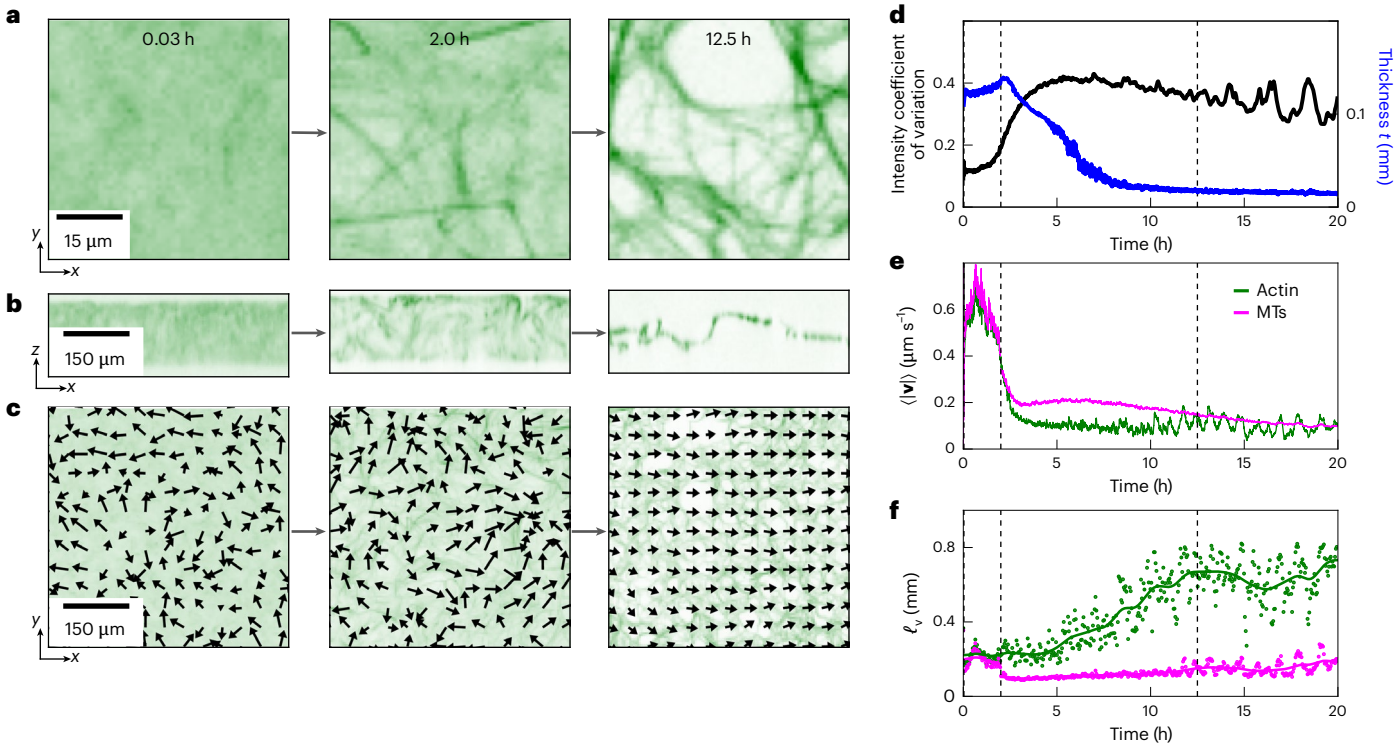

Fig. 3 | Active assembly from a homogeneous suspension. a, Snapshots of actin intensity (*z*-projection of 3D images) normalized by the mean intensity. **b**, Orthogonal slices (*y*-projections) of actin intensity, showing 2D membrane formation. Same time points as in **a**. **c**, Actin velocity field (2D components) overlaid on the *z*-projections. Arrows showing velocity are scaled nonlinearly as $\mathbf{v}/|\mathbf{v}|^{0.7}$ for illustration. **d**, Structural changes of actin over time. Black curve: intensity coefficient of variation (ratio of standard deviation to mean) of the actin fluorescence. Blue curve: mean membrane thickness t. **e**, Time dependence of spatially averaged mean speed $\langle|\mathbf{v}|\rangle$ of MTs and actin. Between 0 h and 2 h, MTs from the entire volume are included in the average. After 2 h, only external MTs are included. **f**, Velocity correlation length ℓ_v of actin and MT velocity fields. 1.5 µM actin, 1.0 µM fascin in active buffer 2. For **d**–**f**, vertical dashed lines indicate time points of the snapshots in **a**–**c**.

−20% and +10% but transiently reached −40% (Supplementary Fig. 1). The deformations were reversible, with the average strain remaining an order of magnitude smaller compared with the transient local strains (Fig. 4g), indicating elastic behaviour. Importantly, the in-plane strain was negatively correlated with local bending; curved membrane sections were more compressed (Fig. 4f–h), indicating that bending was due to buckling of the actin membrane under compression. Moreover, the magnitudes of the mean curvature H and the Gaussian curvature K nearly matched one another (Fig. 4h), providing further evidence that the buckling was the result of geometrically incompatible (non-Euclidean) in-plane strains.

Non-reciprocity drives limit-cycle oscillations and nonlinear waves

As previously noted, the actin membrane deformations became increased correlated over time (Fig. 3f). Low-magnification videos revealed the eventual development of coherent global motion, typically consisting of two counterrotating vortices along the long axis of a sample that periodically reversed direction (Fig. 5a and Supplementary Video 7). Such dynamics emerged from temporally uncorrelated fluctuations, as indicated by the velocity kymograph measured at the centre of the sample along the y axis (Supplementary Fig. 2). To quantify the rotational, compressional and dilational components of the membrane motion, we calculated the vorticity and divergence of the velocity field. The vorticity became correlated across the entire system (Fig. 5b). Relatedly, the power spectrum revealed the dominance of vortical modes at small wavenumbers or long length scales (Fig. 5c). By contrast, correlations in the velocity divergence, indicative of stretching and compression, remained short-range. The associated power spectrum demonstrates that at large length scales, the membrane is effectively incompressible with shear-dominated deformations (Fig. 5c). Notably, the power spectrum of the vorticity modes (enstrophy spectrum) follows a $q^{-3/2}$ power law across almost two orders of magnitude (Fig. 5c), reminiscent of the inverse energy cascade in two-dimensional (2D) turbulence[29]. However, in contrast to inertial turbulence, the dynamics of self-organized membranes is overdamped.

To elucidate the mechanism that powers global oscillations, we measured the actin membrane velocity in the x direction and the average tilt of MT bundles relative to the membrane in the x–z plane (Fig. 5d). The latter yielded a polarization field p_x that encodes the MT tilt direction. The spatially averaged tilt of MT $\langle p_x\rangle$ and the actin membrane velocity $\langle v_x\rangle$ underwent in-phase oscillations (Fig. 5e), indicating that the interplay between these variables drove the oscillations. The tilted extensile MTs drove the lateral membrane motion, which, in turn, further increased the tilt of the MT, resulting in positive feedback (Fig. 5f). With increasing displacement, elastic stresses built up, eventually becoming stronger than the active driving force. The membrane then reversed its motion and subsequently entrained the MT polarity anew until elastic stresses again overcame the driving force, leading to another reversal, thus completing the oscillation cycle.

The MT–membrane interactions are captured by a minimal model that non-reciprocally couples the in-plane displacement u of a membrane patch to the local polarization p describing the MT direction. The balance of forces acting on the overdamped membrane patch reads $\gamma\partial_t u = -k_{\mathrm{eff}}u + f_0 p/(1+|p|/p_0)$, which captures friction due to drag with the surrounding fluid (γ), a spring-like restoring force $-k_{\mathrm{eff}}u$ accounting for the stresses that build up in the membrane and a driving force exerted by the extensile MT bundles. The parameters f_0 and p_0 control the magnitude and saturation of the driving force, respectively. The nonlinearity in the denominator of the driving term saturates the force

https://doi.org/10.1038/s41567-026-03215-5

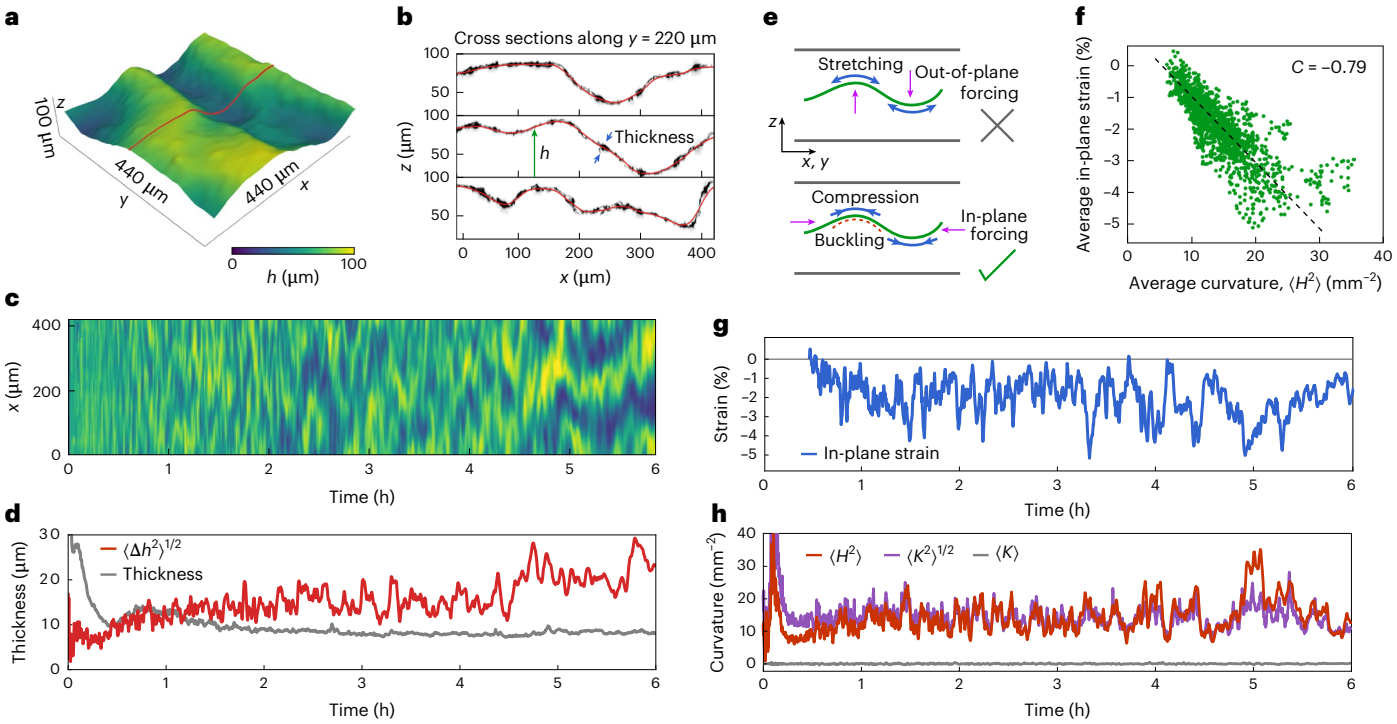

Fig. 4 | Active membrane bending and stretching dynamics. a, Membrane midsurface reconstructed from a 3D image, 3 h after activation. The colour indicates the membrane height h (z-coordinate). **b**, Cross sections corresponding to the red curve in **a** at three consecutive times showing the local actin density (greyscale) and reconstructed midsurface (red lines). **c**, Kymograph of the membrane height h along $y = 220$ µm (red line in **a**). Height fluctuations exhibit a growing timescale. **d**, Time evolution of the average membrane thickness along the local normal (grey line) and root-mean-squared height fluctuation (red line). **e**, Out-of-plane deformation generated through out-of-plane forcing by MTs (top) or through buckling as a result of in-plane forcing by MTs (bottom). **f**, The negative correlation of curvature with strain, indicating that out-of-plane motion is driven by in-plane forcing. Pearson's correlation coefficient $C \approx -0.79$. **g**, Time evolution of the average in-plane strain. Reference displacement at 27.29 min. **h**, Time evolution of the average mean curvature squared $\langle H^2 \rangle$, root-mean-squared Gaussian curvature $\langle K^2 \rangle^{1/2}$ and average Gaussian curvature $\langle K \rangle$. All quantities are averaged over the field of view. Same sample as in Fig. 2.

at large $|p|$. The MT tilt direction p aligns with the membrane motion and decays due to chaotic dynamics: $\partial_t p = -p/\tau_p + \alpha \partial_t u$ with the alignment coefficient α and decay timescale τ_p. Rewriting these equations in matrix form yields

$$\gamma \partial_t \begin{pmatrix} u \\ p \end{pmatrix} = \begin{pmatrix} -k_{\mathrm{eff}} & \frac{f_0}{1+|p|/p_0} \\ -\alpha k_{\mathrm{eff}} & \frac{\alpha f_0}{1+|p|/p_0} - \gamma/\tau_p \end{pmatrix} \begin{pmatrix} u \\ p \end{pmatrix}. \quad (1)$$

In the linear regime ($|p| \ll p_0$), the off-diagonal components with opposite signs indicate antisymmetric coupling between u and p, corresponding to 'run-and-chase' interactions after rescaling of the variables. When $\alpha f_0 > k_{\mathrm{eff}} + \gamma/\tau_p$, the system is linearly unstable and perturbations grow. The nonlinear saturation of the active force eventually results in the limit-cycle oscillations of the local displacement and MT polarization observed in experiments (Supplementary Fig. 3). This mechanism is analogous to what occurs in self-aligning active matter systems, where a polar driving field aligning with the local velocity causes collective motion[30–32] and, more broadly, the emergence of dynamical phases in non-reciprocal many-body systems[33–39].

The minimal model explains the local oscillatory motion but does not describe spatial properties. We extended the model to 2D (Supplementary Information). In short, the restoring force $-k_{\mathrm{eff}}u$ is replaced by an elastic stress $\sigma_{ij}^{\mathrm{el}} = 2\mu u_{ij} + (B-\mu)u_{kk}\delta_{ij}$, where $u_{ij} = (\partial_i u_j + \partial_j u_i)/2$ is the strain tensor and μ and B are, respectively, the shear and bulk moduli. The motion of the membrane relative to the chamber floor and ceiling induces shear in the surrounding fluid, leading to an effective drag force and viscous stress $\sigma_{ij}^{\mathrm{visc}} = 2\eta\partial_t u_{ij} + (\eta_B - \eta)\partial_t u_{kk}\delta_{ij}$, where the shear and bulk viscosities η and η_B are derived using a lubrication approximation[40] (Supplementary Information). This derivation shows that the incompressibility of the bulk fluid causes an effective membrane drag coefficient that is four times higher for compressional modes than for vortical modes. This effective friction arises because compressive deformation of the membrane drags along the surrounding fluid, which then recirculates from the point where the compressive membrane motion converges (Supplementary Fig. 4). The recirculating flow generates a high shear rate along the z direction. The higher friction suppresses the instability of compressional modes relative to the vortical modes, which explains the strong amplification of the large-scale vortical modes observed in experiments (Fig. 5a–c).

The spatially extended model reproduces the wave-like character of the experimentally observed oscillations propagating along the channel (Fig. 5g and Supplementary Video 8). A dispersion relation obtained from the linear stability analysis indicates the growth of wave-like modes (Supplementary Fig. 5). Importantly, these waves are distinct from sound waves originating from inertia and elasticity; they are driven by activity in an overdamped system, with nonlinearities determining the wave amplitude. Furthermore, the linear stability analysis reveals that elastic stresses suppress shorter wavelength modes; therefore, the longest wavelength mode grows the fastest (Supplementary Fig. 5). This explains the transfer of energy from the small-scale driving by MT bundles to the system-sized oscillations that dominate the membrane motion.

Only waves larger than a critical wavelength $\ell_c = 2\pi\ell_{\mathrm{v-el}}/\sqrt{A-1}$ are unstable. Here $A = \alpha f_0 \tau_p$ is the dimensionless driving strength and $\ell_{\mathrm{v-el}} = \sqrt{(\mu\tau_p + \eta)/\gamma}$ is the screening length of viscoelastic stresses in the membrane. Consequently, large-scale unstable modes emerge only

https://doi.org/10.1038/s41567-026-03215-5

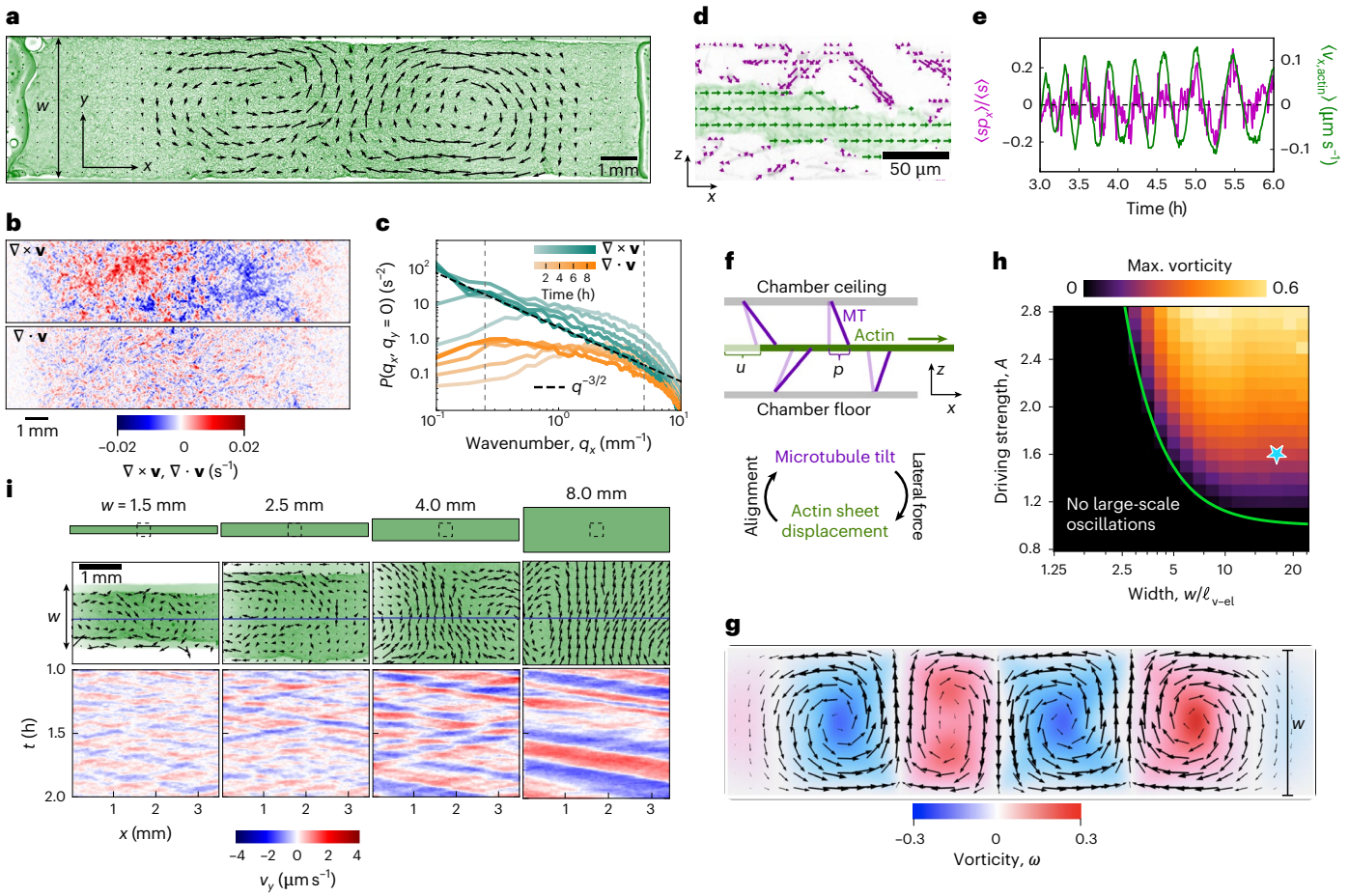

Fig. 5 | System-spanning oscillations. a, Centimetre-sized self-excited actin membrane motion. Arrows show the instantaneous velocity field ($t = 6.75$ h). **b**, Snapshots of the vorticity ($\nabla \times \mathbf{v}$) and divergence ($\nabla \cdot \mathbf{v}$) of the in-plane velocity of the membrane $\mathbf{v}$. **c**, Power spectral density (P) of divergence and vorticity fields over time and calculated along the x axis. Each curve is averaged over 2.2 h. **d**, Polar field of MT bundles calculated from intensity gradients of MTs from the x–z plane. The green arrows indicate actin membrane motion. **e**, Mean lateral MT polarization p_x weighted by MT fluorescence intensity s (magenta) and mean actin membrane lateral velocity v_x (green) plotted over time. **f**, Feedback generates global oscillations. MT bundles align with the membrane motion, which is itself driven by MT forces. The elastic restoring forces provide delayed negative feedback. **g**, Simulation of a nearly incompressible membrane (Supplementary Video 8). **h**, Linear stability analysis predicts sample-width-dependent oscillations. The green line indicates the threshold for oscillations. **i**, Channel width w controls the self-excited dynamics of the actin membranes. Top: velocity fields overlaid on actin fluorescence images. Bottom: kymographs of the v_y component of velocity along the centre line of each sample (blue line). **a**–**c**, 3.2 µM actin, 2.2 µM fascin in active buffer 2. **d**,**e**, 6.0 µM actin, 2.0 µM fascin in active buffer 1. **i**, 3.0 µM actin, 1.0 µM fascin in active buffer 1. Max., maximum.

if the channel width w is larger than half the critical wavelength $\ell_c/2$. As longitudinal modes are suppressed by incompressibility, the channel length is irrelevant for the onset of instability. Thus, the emergence of large-scale waves requires sufficiently wide channels (Fig. 5h). To test this prediction, we studied membranes of various widths (Supplementary Video 9). The presence of wave-like membrane motion was captured by space–time kymographs of $v_y(x, t)$, as evidenced by the sloping bands, which indicate how the velocity maxima (minima) move in space and time (Fig. 5i). Robust travelling-wave dynamics requires membranes wider than 4 mm, thus corroborating the qualitative prediction of the spatially extended model.

Discussion

Our results demonstrate the potential of active assembly, in which life-like materials with complex structure, mechanics and dynamics emerge from a structureless suspension of active and passive components. Previous studies have investigated how molecular motors contract filamentous networks, but these lacked steady-state dynamics[41–46]. Separating the active drive from the passive elastic stresses greatly expands the range of accessible structures while also generating long-term non-equilibrium dynamics.

When combined with the results from other studies[31,47–49], our findings indicate that self-excited waves and oscillations are ubiquitous features of active solids. The active fluid generates elastic membranes and actuates their out-of-plane fluctuations, which we expect to be distinct from the activity-induced fluctuations of fluid-like membranes[50–52]. As exemplified by graphene, such fluctuations greatly increase the effective bending rigidity of the membrane while decreasing its in-plane stretching modulus[53,54]. Analogously, non-thermal fluctuations should also control the mechanics of driven membranes, raising an intriguing scenario in which the increasing out-of-plane fluctuations soften the effective in-plane stiffness, thereby making the membrane more susceptible to global oscillations. Testing this scenario would require models that couple out-of-plane and in-plane deformations.

In a complementary direction, our work raises intriguing analogies with fluid dynamics and turbulence. Chaotic active flows excite floppy modes of a soft network (Supplementary Video 3), which is reminiscent of complex interactions arising between deformable objects and external flows[55]. Like active assembly, turbulent flows enhance the coagulation dynamics in diverse settings, including droplet coalescence in clouds and the accumulation of plankton density in the oceans, with the latter being amplified by the anisotropic plankton shape[56,57]. More

work is needed to quantitatively understand the power-law vorticity spectrum of elastic membranes and possible similarities with classical 2D turbulence[29].

From a materials perspective, active assembly generates fibre networks, an intriguing class of structures that exhibit non-thermal transitions associated with the onset of mechanical rigidity[58–60]. Active stresses continuously actuate and anneal soft modes of the emerging network, thus, perhaps, driving it towards a rigidity transition. The next challenge is to use optically responsive active fluids[61] to design in-plane strains that fold membranes into more complex 3D life-like forms, thus extending work on thin elastic membranes with spatially programmable swelling[62,63].

Active-assembly-like processes might also be relevant in biology. For example, in an activated process, ciliary flows effectively transform large-molecular-weight globular glycoproteins into a Reissner fibre, a tensioned one-dimensional structure that runs down the central canal of the spinal cord and is crucial for developing the straight body axis of many vertebrates[64]. Once assembled, the ciliary flows actuate the non-thermal dynamics of the entire fibre[65]. Similar processes might be relevant in the assembly of viscoelastic mucous and its feedback to the large-scale alignment of the ciliary beating patterns required for the efficient clearance of airway pathways[66].

Online content

Any methods, additional references, Nature Portfolio reporting summaries, source data, extended data, supplementary information, acknowledgements, peer review information; details of author contributions and competing interests; and statements of data and code availability are available at https://doi.org/10.1038/s41567-026-03215-5.

References

1. Cislo, D. J., Pavlopoulos, A. & Shraiman, B. I. 'Morphogenetic action' principle for 3D shape formation by the growth of thin sheets. *Phys. Rev. X* **15**, 021068 (2025).
2. Mitchell, N. P. et al. Visceral organ morphogenesis via calcium-patterned muscle constrictions. *eLife* **11**, e77355 (2022).
3. Nykypanchuk, D., Maye, M. M., van der Lelie, D. & Gang, O. DNA-guided crystallization of colloidal nanoparticles. *Nature* **451**, 549–552 (2008).
4. Douglas, S. M. et al. Self-assembly of DNA into nanoscale three-dimensional shapes. *Nature* **459**, 414–418 (2009).
5. Jacobs, W. M., Reinhardt, A. & Frenkel, D. Rational design of self-assembly pathways for complex multicomponent structures. *Proc. Natl Acad. Sci. USA* **112**, 6313–6318 (2015).
6. He, M. et al. Colloidal diamond. *Nature* **585**, 524–529 (2020).
7. Wei, W.-S. et al. Hierarchical assembly is more robust than egalitarian assembly in synthetic capsids. *Proc. Natl Acad. Sci. USA* **121**, e2312775121 (2024).
8. Whitelam, S. & Jack, R. L. The statistical mechanics of dynamic pathways to self-assembly. *Annu. Rev. Phys. Chem.* **66**, 143 (2015).
9. Keren, K. et al. Mechanism of shape determination in motile cells. *Nature* **453**, 475 (2008).
10. Brugués, J. & Needleman, D. Physical basis of spindle self-organization. *Proc. Natl Acad. Sci. USA* **111**, 18496 (2014).
11. Aditi Simha, R. & Ramaswamy, S. Hydrodynamic fluctuations and instabilities in ordered suspensions of self-propelled particles. *Phys. Rev. Lett.* **89**, 058101 (2002).
12. Sanchez, T., Chen, D. T., DeCamp, S. J., Heymann, M. & Dogic, Z. Spontaneous motion in hierarchically assembled active matter. *Nature* **491**, 431 (2012).
13. Wensink, H. H. et al. Meso-scale turbulence in living fluids. *Proc. Natl Acad. Sci. USA* **109**, 14308 (2012).
14. Zhou, S., Sokolov, A., Lavrentovich, O. D. & Aranson, I. S. Living liquid crystals. *Proc. Natl Acad. Sci. USA* **111**, 1265–1270 (2014).
15. Wu, X.-L. & Libchaber, A. Particle diffusion in a quasi-two-dimensional bacterial bath. *Phys. Rev. Lett.* **84**, 3017–3020 (2000).
16. Di Leonardo, R. et al. Bacterial ratchet motors. *Proc. Natl Acad. Sci. USA* **107**, 9541 (2010).
17. Sokolov, A., Apodaca, M. M., Grzybowski, B. A. & Aranson, I. S. Swimming bacteria power microscopic gears. *Proc. Natl Acad. Sci. USA* **107**, 969 (2010).
18. Jia, H. et al. 3D printed protein-based robotic structures actuated by molecular motor assemblies. *Nat. Mater.* **21**, 703–709 (2022).
19. Grober, D. et al. Unconventional colloidal aggregation in chiral bacterial baths. *Nat. Phys.* **19**, 1680–1688 (2023).
20. Pedersen, M. C., Mukherjee, S., Doostmohammadi, A., Mondal, C. & Thijssen, K. Active particles knead three-dimensional gels into porous structures. *Phys. Rev. Lett.* **133**, 228301 (2024).
21. Frechette, L. B., Baskaran, A. & Hagan, M. F. Active-noise-induced dynamic clustering of passive colloidal particles. *Newton* **1**, 100167 (2025).
22. Martinet, Q., Li, Y., Aubret, A., Hannezo, E. & Palacci, J. Emergent dynamics of active elastic microbeams. *Phys. Rev. X* **15**, 041017 (2025).
23. Lieleg, O., Claessens, M. M. A. E., Heussinger, C., Frey, E. & Bausch, A. R. Mechanics of bundled semiflexible polymer networks. *Phys. Rev. Lett.* **99**, 088102 (2007).
24. Kayser, J., Grabmayr, H., Harasim, M., Herrmann, H. & Bausch, A. R. Assembly kinetics determine the structure of keratin networks. *Soft Matter* **8**, 8873 (2012).
25. Falzone, T. T., Lenz, M., Kovar, D. R. & Gardel, M. L. Assembly kinetics determine the architecture of α-actinin crosslinked F-actin networks. *Nat. Commun.* **3**, 861 (2012).
26. Foffano, G., Levernier, N. & Lenz, M. The dynamics of filament assembly define cytoskeletal network morphology. *Nat. Commun.* **7**, 13827 (2016).
27. Berezney, J., Goode, B. L., Fraden, S. & Dogic, Z. Extensile to contractile transition in active microtubule-actin composites generates layered asters with programmable lifetimes. *Proc. Natl Acad. Sci. USA* **119**, e2115895119 (2022).
28. Chandrakar, P. et al. Engineering stability, longevity, and miscibility of microtubule-based active fluids. *Soft Matter* **18**, 1825–1835 (2022).
29. Paret, J. & Tabeling, P. Experimental observation of the two-dimensional inverse energy cascade. *Phys. Rev. Lett.* **79**, 4162 (1997).
30. Shimoyama, N., Sugawara, K., Mizuguchi, T., Hayakawa, Y. & Sano, M. Collective motion in a system of motile elements. *Phys. Rev. Lett.* **76**, 3870 (1996).
31. Baconnier, P. et al. Selective and collective actuation in active solids. *Nat. Phys.* **18**, 1234–1239 (2022).
32. Baconnier, P. et al. Self-aligning polar active matter. *Rev. Mod. Phys.* **97**, 015007 (2025).
33. You, Z., Baskaran, A. & Marchetti, M. C. Nonreciprocity as a generic route to traveling states. *Proc. Natl Acad. Sci. USA* **117**, 19767 (2020).
34. Scheibner, C. et al. Odd elasticity. *Nat. Phys.* **16**, 475 (2020).
35. Saha, S., Agudo-Canalejo, J. & Golestanian, R. Scalar active mixtures: the nonreciprocal Cahn-Hilliard model. *Phys. Rev. X* **10**, 041009 (2020).
36. Fruchart, M., Hanai, R., Littlewood, P. B. & Vitelli, V. Non-reciprocal phase transitions. *Nature* **592**, 363 (2021).
37. Tan, T. H. et al. Odd dynamics of living chiral crystals. *Nature* **607**, 287 (2022).
38. Gu, F., Guiselin, B., Bain, N., Zuriguel, I. & Bartolo, D. Emergence of collective oscillations in massive human crowds. *Nature* **638**, 112 (2025).

39. Fructhart, M., Vitelli, V. Nonreciprocal many-body physics. preprint available at https://arxiv.org/abs/2602.11111
40. Oron, A., Davis, S. H. & Bankoff, S. G. Long-scale evolution of thin liquid films. *Rev. Mod. Phys.* **69**, 931 (1997).
41. Köhler, S., Schaller, V. & Bausch, A. R. Structure formation in active networks. *Nat. Mater.* **10**, 462 (2011).
42. Murrell, M. P. & Gardel, M. L. F-actin buckling coordinates contractility and severing in a biomimetic actomyosin cortex. *Proc. Natl Acad. Sci. USA* **109**, 20820–20825 (2012).
43. Alvarado, J., Sheinman, M., Sharma, A., MacKintosh, F. C. & Koenderink, G. H. Molecular motors robustly drive active gels to a critically connected state. *Nat. Phys.* **9**, 591–597 (2013).
44. Foster, P. J., Fürthauer, S., Shelley, M. J. & Needleman, D. J. Active contraction of microtubule networks. *eLife* **4**, e10837 (2015).
45. Lee, G. et al. Myosin-driven actin-microtubule networks exhibit self-organized contractile dynamics. *Sci. Adv.* **7**, eabe4334 (2021).
46. Livne, G., Gat, S., Armon, S. & Bernheim-Groswasser, A. Self-assembled active actomyosin gels spontaneously curve and wrinkle similar to biological cells and tissues. *Proc. Natl Acad. Sci. USA* **121**, e2309125121 (2024).
47. Hemingway, E. et al. Active viscoelastic matter: from bacterial drag reduction to turbulent solids. *Phys. Rev. Lett.* **114**, 098302 (2015).
48. Liu, S., Shankar, S., Marchetti, M. C. & Wu, Y. Viscoelastic control of spatiotemporal order in bacterial active matter. *Nature* **590**, 80–84 (2021).
49. Levanon, M. et al. Active flow-driven DNA remodeling generates millimeter-scale mechanical oscillations. Preprint at http://arxiv.org/abs/2511.22589 (2025).
50. Turlier, H. et al. Equilibrium physics breakdown reveals the active nature of red blood cell flickering. *Nat. Phys.* **12**, 513–519 (2016).
51. Vutukuri, H. R. et al. Active particles induce large shape deformations in giant lipid vesicles. *Nature* **586**, 52–56 (2020).
52. Sciortino, A. et al. Active membrane deformations of a minimal synthetic cell. *Nat. Phys.* **21**, 799–807 (2025).
53. Nelson, D. & Peliti, L. Fluctuations in membranes with crystalline and hexatic order. *J. Phys.* **48**, 1085 (1987).
54. Blees, M. K. et al. Graphene kirigami. *Nature* **524**, 204–207 (2015).
55. Zhang, J., Childress, S., Libchaber, A. & Shelley, M. Flexible filaments in a flowing soap film as a model for one-dimensional flags in a two-dimensional wind. *Nature* **408**, 835 (2000).
56. Saffman, P. & Turner, J. On the collision of drops in turbulent clouds. *J. Fluid Mech.* **1**, 16 (1956).
57. Arguedas-Leiva, J.-A., Słomka, J., Lalescu, C. C., Stocker, R. & Wilczek, M. Elongation enhances encounter rates between phytoplankton in turbulence. *Proc. Natl Acad. Sci. USA* **119**, e2203191119 (2022).
58. Broedersz, C. P., Mao, X., Lubensky, T. C. & MacKintosh, F. C. Criticality and isostaticity in fibre networks. *Nat. Phys.* **7**, 983–988 (2011).
59. Sharma, A. et al. Strain-controlled criticality governs the nonlinear mechanics of fibre networks. *Nat. Phys.* **12**, 584–587 (2016).
60. Bantawa, M. et al. The hidden hierarchical nature of soft particulate gels. *Nat. Phys.* **19**, 1178–1184 (2023).
61. Ross, T. D. et al. Controlling organization and forces in active matter through optically defined boundaries. *Nature* **572**, 224 (2019).
62. Klein, Y., Efrati, E. & Sharon, E. Shaping of elastic sheets by prescription of non-Euclidean metrics. *Science* **315**, 1116–1120 (2007).
63. Kim, J., Hanna, J. A., Byun, M., Santangelo, C. D. & Hayward, R. C. Designing responsive buckled surfaces by halftone gel lithography. *Science* **335**, 1201–1205 (2012).
64. Bearce, E. A. et al. Motile cilia spin the Reissner fiber, a tensioned and anchored extracellular thread essential for body morphogenesis. Preprint at *bioRxiv* https://doi.org/10.1101/2025.09.25.678623 (2025).
65. Bellegarda, C. et al. The Reissner fiber under tension in vivo shows dynamic interaction with ciliated cells contacting the cerebrospinal fluid. *eLife* **12**, e86175 (2023).
66. Loiseau, E. et al. Active mucus–cilia hydrodynamic coupling drives self-organization of human bronchial epithelium. *Nat. Phys.* **16**, 1158 (2020).
67. Ray, S., Berezney, J. & Kolvin, I. Data for: Active assembly and non-reciprocal dynamics of elastic membranes. *Zenodo* https://doi.org/10.5281/zenodo.17215226 (2025).

Reporting summary

Further information on research design is available in the Nature Portfolio Reporting Summary linked to this article.

Data availability

Representative data from this study are available via Zenodo at https://doi.org/10.5281/zenodo.17215226 (ref. 67). Source data are provided with this paper.

Code availability

The code used for data analysis is available via Zenodo at https://doi.org/10.5281/zenodo.17215226 (ref. 67).

Acknowledgements

We thank L. Frechette, B. Chakraborty and X. Mao for insightful discussions. This work was primarily supported by the US Department of Energy (Grant No. DE-SC0022291 to J.B., S.R., I.K., S.F. and Z.D.). F.B. acknowledges support from a Gordon and Betty Moore post-doctoral fellowship (Award No. 2919). The theoretical work was supported in part by the National Science Foundation through Grant No. PHY-2309135 to the Kavli Institute for Theoretical Physics (M.B.). V.V. and S.C. acknowledge partial support from the Army Research Office (Grant Nos. W911NF-22-2-0109 and W911NF-23-1-0212), the National Science Foundation through the Center for Living Systems (Grant No. 2317138), the National Institute for Theory and Mathematics in Biology, the Simons Foundation and the Chan Zuckerberg Foundation.

Author contributions

J.B., S.R., I.K. and Z.D. conceptualized the work. J.B., S.R. and I.K. performed the experiments. J.B., S.R., I.K. and F.B. analysed the data. F.B., S.C., M.B. and V.V. developed the theoretical analysis. All authors contributed to the writing of the paper.

Competing interests

The authors declare no competing interests.

Additional information

Supplementary information The online version contains supplementary material available at https://doi.org/10.1038/s41567-026-03215-5.

Correspondence and requests for materials should be addressed to Zvonimir Dogic.

Peer review information *Nature Physics* thanks Jennifer Ross and Ishant Tiwari for their contribution to the peer review of this work. Peer reviewer reports are available.

nature portfolio

Corresponding author(s): Zvonimir Dogic

Last updated by author(s): 2026-31-01

Reporting Summary

Nature Portfolio wishes to improve the reproducibility of the work that we publish. This form provides structure for consistency and transparency in reporting. For further information on Nature Portfolio policies, see our Editorial Policies and the Editorial Policy Checklist.

Statistics

For all statistical analyses, confirm that the following items are present in the figure legend, table legend, main text, or Methods section.

n/a	Confirmed
☐	☒ The exact sample size (*n*) for each experimental group/condition, given as a discrete number and unit of measurement
☐	☒ A statement on whether measurements were taken from distinct samples or whether the same sample was measured repeatedly
☒	☐ The statistical test(s) used AND whether they are one- or two-sided *Only common tests should be described solely by name; describe more complex techniques in the Methods section.*
☒	☐ A description of all covariates tested
☐	☒ A description of any assumptions or corrections, such as tests of normality and adjustment for multiple comparisons
☒	☐ A full description of the statistical parameters including central tendency (e.g. means) or other basic estimates (e.g. regression coefficient) AND variation (e.g. standard deviation) or associated estimates of uncertainty (e.g. confidence intervals)
☒	☐ For null hypothesis testing, the test statistic (e.g. *F*, *t*, *r*) with confidence intervals, effect sizes, degrees of freedom and *P* value noted *Give P values as exact values whenever suitable.*
☒	☐ For Bayesian analysis, information on the choice of priors and Markov chain Monte Carlo settings
☒	☐ For hierarchical and complex designs, identification of the appropriate level for tests and full reporting of outcomes
☒	☐ Estimates of effect sizes (e.g. Cohen's *d*, Pearson's *r*), indicating how they were calculated

Our web collection on statistics for biologists contains articles on many of the points above.

Software and code

Policy information about availability of computer code

Data collection	Image sequences were acquired from microscopes using MicroManager 1.4 (for widefield imaging) and NIS-Elements (for confocal imaging).
Data analysis	3D image was rendered using Imaris. Velocity fields were computed using PIVLab v.3. Network nodes were tracked using TrackPy. Simulations were performed in COMSOL. All other analysis was done using custom code that will be available on Zenodo (https://doi.org/10.5281/zenodo.17215226) or upon request.

For manuscripts utilizing custom algorithms or software that are central to the research but not yet described in published literature, software must be made available to editors and reviewers. We strongly encourage code deposition in a community repository (e.g. GitHub). See the Nature Portfolio guidelines for submitting code & software for further information.

Data

Policy information about availability of data

All manuscripts must include a data availability statement. This statement should provide the following information, where applicable:

- Accession codes, unique identifiers, or web links for publicly available datasets
- A description of any restrictions on data availability
- For clinical datasets or third party data, please ensure that the statement adheres to our policy

Data will be available on Zenodo (https://doi.org/10.5281/zenodo.17215226) or upon request.

Research involving human participants, their data, or biological material

Policy information about studies with human participants or human data. See also policy information about sex, gender (identity/presentation), and sexual orientation and race, ethnicity and racism.

Reporting on sex and gender	*Use the terms sex (biological attribute) and gender (shaped by social and cultural circumstances) carefully in order to avoid confusing both terms. Indicate if findings apply to only one sex or gender; describe whether sex and gender were considered in study design; whether sex and/or gender was determined based on self-reporting or assigned and methods used.* *Provide in the source data disaggregated sex and gender data, where this information has been collected, and if consent has been obtained for sharing of individual-level data; provide overall numbers in this Reporting Summary. Please state if this information has not been collected.* *Report sex- and gender-based analyses where performed, justify reasons for lack of sex- and gender-based analysis.*
Reporting on race, ethnicity, or other socially relevant groupings	*Please specify the socially constructed or socially relevant categorization variable(s) used in your manuscript and explain why they were used. Please note that such variables should not be used as proxies for other socially constructed/relevant variables (for example, race or ethnicity should not be used as a proxy for socioeconomic status).* *Provide clear definitions of the relevant terms used, how they were provided (by the participants/respondents, the researchers, or third parties), and the method(s) used to classify people into the different categories (e.g. self-report, census or administrative data, social media data, etc.)* *Please provide details about how you controlled for confounding variables in your analyses.*
Population characteristics	*Describe the covariate-relevant population characteristics of the human research participants (e.g. age, genotypic information, past and current diagnosis and treatment categories). If you filled out the behavioural & social sciences study design questions and have nothing to add here, write "See above."*
Recruitment	*Describe how participants were recruited. Outline any potential self-selection bias or other biases that may be present and how these are likely to impact results.*
Ethics oversight	*Identify the organization(s) that approved the study protocol.*

Note that full information on the approval of the study protocol must also be provided in the manuscript.

Field-specific reporting

Please select the one below that is the best fit for your research. If you are not sure, read the appropriate sections before making your selection.

☒ Life sciences ☐ Behavioural & social sciences ☐ Ecological, evolutionary & environmental sciences

For a reference copy of the document with all sections, see nature.com/documents/nr-reporting-summary-flat.pdf

Life sciences study design

All studies must disclose on these points even when the disclosure is negative.

Sample size	in the manuscript we describe analysis and behavior of active assembly for several different assembly conditions. Our work does not involve statistical analysis
Data exclusions	there were no data exclusions
Replication	we repeated sweeps of relevant experimental parameters including actin concentration and buffer composition several times. We observer reproducible behavior across different parameters sweeps. In the manuscript we describe the behavior of representative samples.
Randomization	randomization was not possible. We describe behavior of several different samples and how their dynamics over time. The results of our manuscript does not involve statistical analysis.
Blinding	blinding is not possible with the nature of the experimental data that is being acquired and analyzed

Reporting for specific materials, systems and methods

We require information from authors about some types of materials, experimental systems and methods used in many studies. Here, indicate whether each material, system or method listed is relevant to your study. If you are not sure if a list item applies to your research, read the appropriate section before selecting a response.

Materials & experimental systems

n/a	Involved in the study
☒	☐ Antibodies
☒	☐ Eukaryotic cell lines
☒	☐ Palaeontology and archaeology
☒	☐ Animals and other organisms
☒	☐ Clinical data
☒	☐ Dual use research of concern
☒	☐ Plants

Methods

n/a	Involved in the study
☒	☐ ChIP-seq
☒	☐ Flow cytometry
☒	☐ MRI-based neuroimaging

Plants

Seed stocks

Report on the source of all seed stocks or other plant material used. If applicable, state the seed stock centre and catalogue number. If plant specimens were collected from the field, describe the collection location, date and sampling procedures.

Novel plant genotypes

Describe the methods by which all novel plant genotypes were produced. This includes those generated by transgenic approaches, gene editing, chemical/radiation-based mutagenesis and hybridization. For transgenic lines, describe the transformation method, the number of independent lines analyzed and the generation upon which experiments were performed. For gene-edited lines, describe the editor used, the endogenous sequence targeted for editing, the targeting guide RNA sequence (if applicable) and how the editor was applied.

Authentication

Describe any authentication procedures for each seed stock used or novel genotype generated. Describe any experiments used to assess the effect of a mutation and, where applicable, how potential secondary effects (e.g. second site T-DNA insertions, mosiacism, off-target gene editing) were examined.